Effects of quenching on phase transformations and ferroelectric properties of 0.35BCZT-0.65KBT ceramics

AL-AARAJI, M.N., FETEIRA, Antonio <http://orcid.org/0000-0001-8151-7009>, THOMPSON, S.P., MURRAY, C.A. and HALL, D.A.

Title: Effects of quenching on phase transformations and ferroelectric properties of 0.35BCZT-0.65KBT ceramics

Authors: Mohammed N. Al-Aaraji, Antonio Feteira, Stephen P. Thompson, Claire A. Murray, David A. Hall

PII: S0955-2219(19)30432-7
DOI: https://doi.org/10.1016/j.jeurceramsoc.2019.06.016
Reference: JECS 12573

To appear in: *Journal of the European Ceramic Society*

Received date: 22 February 2019
Revised date: 6 June 2019
Accepted date: 7 June 2019

Please cite this article as: Al-Aaraji MN, Feteira A, Thompson SP, Murray CA, Hall DA, Effects of quenching on phase transformations and ferroelectric properties of 0.35BCZT-0.65KBT ceramics, *Journal of the European Ceramic Society* (2019), https://doi.org/10.1016/j.jeurceramsoc.2019.06.016

Effects of quenching on phase transformations and ferroelectric properties of 0.35BCZT-0.65KBT ceramics.

Mohammed N. Al-Aaraji[1,2], Antonio Feteira[3], Stephen P. Thompson[4], Claire A. Murray[4], and David A. Hall[1]

[1] School of Materials, University of Manchester, M13 9PL, Manchester, U.K.
[2] Ceramics and Construction Materials Department, College of Materials Engineering University of Babylon, Al Hilla, Iraq.
[3] Christian Doppler Lab for Advanced Ferroic Oxides, Materials and Engineering Research Institute, Sheffield Hallam University, S1 1WB, UK.
[4] Diamond Light Source Ltd, Diamond House, Harwell Science and Innovation Campus, Didcot, Oxfordshire OX11 0DE, UK.

Abstract

Solid solutions of 0.35(Ba,Ca)(Zr,Ti)O_3-0.65($K_{0.5}Bi_{0.5}$)TiO_3 (BCZT-KBT) having various Ca and Zr contents were synthesized by solid state reaction. The sintered ceramics exhibited interesting features comprising core-shell type microstructures and relaxor ferroelectric behaviour. The influence of air-quenching on structure and electrical properties has been systematically investigated. The results indicate that the compositional heterogeneity in the shell regions, for the slow-cooled state, was reduced by air quenching. Improvements are evident in ferroelectric tetragonal phase content, accompanied by increased polarisation values and depolarisation temperatures. Comparing the results obtained for two BCZT compositions, it was demonstrated that the stability of the ferroelectric tetragonal phase in slow-cooled BCZT-KBT samples was improved for the ceramic with lower Ca and Zr concentrations, denoted x=0.06, comparing with that for higher levels, denoted x=0.15. Furthermore, the electric field-induced ferroelectric state in the quenched ceramic with x=0.06 was found to be more stable during heating, yielding an enhanced depolarisation temperature.

Keywords: Lead-free ceramics; Ferroelectrics; Core-Shell; Relaxors.

1 Introduction

Relaxor ferroelectric materials are classified as ferroelectrics, but display additional or different functional behaviour in comparison with *normal ferroelectrics*. They are characterised by random occupation of one or more ions in the equivalent site within

the unit cell [1]. This disordered distribution generates unique structural and functional properties [2]. Based on crystal structure, oxide relaxors can be divided into two types, which are either the tungsten-bronze structure, $(A1)_2(A2)_4(C)_4(B1)_2(B2)_8O_{30}$ or the perovskite structure, ABO_3. The A- and B-sites within the perovskite structure can be occupied by more than one type of ion, denoted $(A'A'')(B'B'')O_3$, [3, 4]. They are also commonly formed from *complex* perovskites, where the A- or B-sites contain ions having different valence states [5]. $PbMg_{1/3}Nb_{2/3}O_3$ (PMN) and $Pb(Zn_{1/3}Nb_{2/3})O_3$ (PZN) are typical examples of complex lead-based perovskites while $BaTiO_3$-$BaSnO_3$ is a lead-free relaxor that was first reported by Smolensky [6]. However, research has generally focused on lead-free materials in recent years, due to environmental concerns [7, 8]. Furthermore, the existence of polar clusters or *polar nanoregions* (PNRs) in relaxors is considered as their most important characteristic structural feature[9]. It is believed that this feature is the key to understanding the origin of relaxor ferroelectric properties [10]. Based on the stability of dipoles within PNRs, the relaxors can have two different states. One is a *non-ergodic* state, in which the transformation from polar nanoregions (PNRs) to ordered ferroelectric domains under application of an external excitation is irreversible. The other is the *ergodic* state which is associated with a more reversible transformation between PNRs and ordered ferroelectric domains [11, 12]. The main external excitations are: electric field, mechanical load and temperature, any of which could induce metastable ferroelectric order in relaxors. However, the stability of an induced transformation after removal of the external excitation depends on the nature of the PNRs.

The *ergodic* state in relaxors represents the main reason for their reported 'giant' electro-mechanical response [13, 14]. Therefore, many researchers have attempted to induce the ergodic relaxor state intentionally by compositional modification such as the addition of dopants [15-19]. Bismuth-based perovskite relaxors such as BNT ($Bi_{0.5}Na_{0.5}TiO_3$) and related materials are prime examples of such behaviour [13, 14]. This characteristic was also observed in $K_{0.5}Bi_{0.5}TiO_3$-doped $(Ba,Ca)(Zr,Ti)O_3$, BCZT-KBT [20]. Large electromechanical strains of up to 0.43% (S_{max}/E_{max}= 621 pm/V) have been generated in $xBi(Mg_{0.5}Ti_{0.5})O_3–(0.75−x)PbTiO_3–0.25(Bi_{0.5}Na_{0.5})TiO_3$ ternary solid solutions at the MPB region with $0.50 < x < 0.51$, where the coexistence of tetragonal and pseudocubic phases was reported, leading to an *ergodic* relaxor ferroelectric state [21].

Several recent studies [22-24] reported that the compositionally-induced transition from long-range ordered ferroelectric to pseudocubic relaxor phases was accompanied by the development of core-shell type microstructure, with ferroelectric domains in the core regions being embedded within a relaxor ferroelectric shell. Calisir [25] observed that the type of ionic substitution also has a profound influence on microstructure. Both isovalent and donor substitutions of La^{3+}, for Bi^{3+} and Ba^{2+} respectively, were investigated in the solid solution $0.75BiFeO_3$-$0.25BaTiO_3$ (75BFBT). The results showed that 1 mol% donor substitution of La^{3+} for Ba^{2+} in 75BFBT ceramics induced the formation of core-shell type microstructures comprising $BiFeO_3$-rich core and $BaTiO_3$-rich shell regions. In contrast, more

homogeneous microstructures with well-ordered ferroelectric domain patterns were clearly observed throughout the grains for the case of isovalent substitution of La^{3+} for Bi^{3+}. Application of an electric field induces phase transitions in both the core and shell regions. However, the core remains in a poled state after field removal, while the shell is characterized by a reversible transformation. Therefore, the development of such core–shell structures was considered to play a significant role in achievement of a high reversible electromechanical strain [21, 26]. For example, an electric field-induced strain of ~0.3% at 4 kV/mm was reported for $Bi_{1/2}Na_{1/2}TiO_3$–$SrTiO_3$ ceramics having a core-shell structure by Acosta [26]. Based on these findings, it was proposed that the proper design of a core–shell material could lead to modifications of strain output, hysteresis, temperature stability and fatigue behaviour.

In recent publications, it has been reported that heat treatment of bismuth-based perovskites by thermal quenching (rapid cooling) could induce structural transformations, relaxation of the lattice strain and randomisation of the defect dipole orientations, leading to improved thermal stability of ferroelectric properties [27-29]. It was found that use of a quenching process increased the depolarization temperature, T_d, of BNT ceramics from 173 °C to 223 °C [30] and improved the remanent polarisation, P_r, of MnO_2-modified $0.75BiFeO_3$–$0.25BaTiO_3$ ceramics from 0.06 to 0.31 C m^{-2} [31].

In the present study, novel compositions based on 0.35BCZT-0.65KBT solid solutions were prepared using solid state reaction. Two BCZT compositions were used, based on the formula $(Ba_{1-x}Ca_x)(Ti_{1-y}Zr_y)O_3$, with different Ca and Zr contents. These BCZT compositions were selected on the basis of their attractive piezoelectric properties due to the coexistence of the orthorhombic and tetragonal phases that resulted from the optimized substitution of the Ba- and Ti-sites with low and high levels of Ca, Zr ions respectively, as reported previously [32-34]. We also aim to investigate how variations in the stoichiometry of the BCZT component influence the phase stability of the solid solution, BCZT-KBT, under heating and application of an electric field. This contribution focuses on the influence of quenching on structure and ferroelectric behaviour of these ceramic materials, with the aim of increasing the depolarisation temperature and controlling the ferroelectric properties by modifying the thermal processing parameters. We propose that chemical homogeneity could be improved by this type of heat treatment, which leads to enhanced ferroelectric switching characteristics and increased depolarisation temperatures. On the other hand, higher reversible field-induced strain values can be obtained for ceramics in the slow-cooled state due to the presence of PNRs in an *ergodic* state in the shell regions.

2 Experimental procedures

Based on the formula $Ba_{1-x}\ Ca_x\ (Ti_{1-y}\ Zr_y)\ O_3$, two BCZT solid solutions with x=0.06, y=0.07 [32] and x=0.15, y=0.1[33, 34] were prepared in the form of polycrystalline ceramics using the solid state reaction method. Barium carbonate ($BaCO_3$, Alfa Aesar Co. 99% purity), calcium carbonate ($CaCO_3$, Sigma Aldrich ≥ 99.0 % purity), titanium dioxide (TiO_2, Huntsman A-HR 99% purity), and zirconium oxide (ZrO_2, Magnesium Elektron E-101) were used as raw materials. The raw powders were

weighed according to the stoichiometry of the selected compositions. They were vibro-ball milled with propan-2-ol for 24 h using zirconia balls, 5 mm in diameter, as milling media. After drying, the mixed powders were calcined at 1300 °C for 4 h in a covered alumina crucible. A pure $K_{0.5}Bi_{0.5}TiO_3$ powder was prepared, in parallel, using potassium carbonate (K_2CO_3, Fluka ≥ 99.0 % purity), bismuth oxide (Bi_2O_3, Alfa Aesar 99.0 % purity) and titanium dioxide (TiO_2, Huntsman A-HR 99% purity) as raw materials. After weighing, ball-milling in the above manner and drying of powders, the mixture was calcined at 950 °C for 4 h.

Afterward, the calcined BCZT powders were mixed separately with KBT and 2 wt% of excess bismuth oxide in order to compensate for any loss via volatilization during subsequent sintering at elevated temperatures. This specific level of excess bismuth oxide was selected on the basis of results obtained from an investigation into the effects of the bismuth oxide excess on the properties of BCZT-KBT ceramics, which demonstrated that, using the present processing procedures, 2 wt.% of excess Bi_2O_3 was the optimal content to produce ceramics free of second phases.

The mixed powders were ball-milled for 72 h, followed by drying and mixing with 2 wt% polyethylene glycol solution (PEG 1500) as a lubricant and binder. Subsequently, the mixed calcined powders including binder were uniaxially pressed in a 10 mm diameter cylindrical steel die into pellets having a thickness ~1.5 mm, under a pressure of 150 MPa for 40 s. The pellets were placed inside a covered alumina crucible for sintering on a thin layer of zirconia sand (baddeleyite) to avoid any interfacial reactions between the ceramic disks and the supporting alumina base. The pellets were heated up first to 500 °C, with 1 h dwell time to burn-out the organic additive; thereafter the temperature was raised to 1125 °C with a 3 h dwell for sintering. The heating/ cooling rate was 5 °C min^{-1}.

The bulk densities of the sintered samples were measured by the Archimedes method using water as the immersion medium. For structural and electrical characterization, the surfaces of the sintered samples were ground using 1200-grade SiC paper to obtain parallel and smooth faces. Then, the samples were annealed at 500 °C for 30 min to minimise any residual stresses that could be induced during preparation. These ceramics are denoted *slow-cooled (SC)* samples. Some of these samples were subsequently heated to 1000 °C for 1 h and then quenched in air; these are denoted *quenched (Q)* samples.

The sintered ceramic pellets were coated with silver paste (C2000107P3, Gwent Electronic Materials) for electrical measurements. The painted samples were dried in an oven at 85 °C for 20 min for each face and then heat treated at 550 °C for 30 min to densify the electrodes and ensure intimate contact with the ceramic surfaces. Polarization-electric field (P-E) ferroelectric hysteresis measurements were made using a system based on a HP33120A function generator (Hewlett-Packard, Palo Alto, CA) in conjunction with an HVA1B high voltage amplifier (Chevin Research, Otley, UK) [35]. A burst-mode waveform comprising 4 sinusoidal cycles was employed, with a maximum electric field level up to 6 MV m^{-1}. The samples were immersed in silicone oil during these measurements to avoid electrical arcing. For SXPD studies

on the poled ceramics, specimens were instead electroded using an air-dried silver paint (AGG3691, Agar scientific), which was removed after poling using acetone. The quenched samples that were produced by this process are denoted *quenched-poled* (*QP*).

The measurement of strain-electric field, *x-E*, loops was carried out as a function of temperature under an alternating bipolar electric field using an AixACCT TF 2000 Ferroelectric Analyzer, using a triangular waveform with a frequency of 1 Hz. Strain was calculated from the electric-field displacement, which was measured using a laser interferometer (SIOS MeβTechnik, GmbH, Type SP-S 120).

Variations in the low-field dielectric properties of the sintered samples as a function of temperature and frequency were determined using an automated dielectric measurement system comprising an LCR-meter (Hewlett-Packard Precision LCR Meter, HP 4284A) connected to the electroded sample by pure silver probes. Samples were heated in a furnace with a heating rate of 2 °C min^{-1}. The parallel capacitance, C_p, and the dielectric loss tangent, tan δ, were measured over the temperature range from 25 to 350 °C, at frequencies from 1 kHz to 100 kHz.

For depolarization temperature, T_d, measurements, the thermally stimulated depolarization current (TSDC) method was employed to determine the T_d directly, as described in a previous study [36]. In this approach, the depolarisation current, I_{dep}, for a poled sample is measured during heating; these values are divided by the cross-sectional surface area, *A*, to obtain the depolarisation current density, J_{dep} . The latter is plotted as a function of temperature to identify the temperature at which the sharpest change in polarisation occurs, and this represents the T_d. Therefore, in the present work, the poled ceramic pellets were placed into a temperature-controlled tube furnace (Carbolite MTF 1200). The measurements were taken at a heating rate of 2 °C min^{-1} and the temperature was recorded with a thermocouple placed next to the pellet. The pyroelectric current was determined using a current amplifier [35]. The electric charge released was calculated by integration of the current over time and converted into a change in remanent polarisation, ΔP, calculated in terms of the surface charge density.

High resolution synchrotron x-ray diffraction (SXPD) measurements were performed at beamline I11, Diamond Light Source Ltd., UK [37]. The slow-cooled, quenched and quenched-poled samples were crushed and ground to fine powder using a pestle and mortar. Then, the powder samples were packed into 0.3 mm diameter borosilicate glass capillaries. Due to the high bismuth content, a photon energy of 25 keV was selected in order to reduce the effects of specimen absorption; the wavelength of 0.494216 Å was calibrated using NIST 640C SiC powder. The angular range was scanned from 5 to 90º 2θ and the diffracted intensities were recorded using the beamline's wide-angle position sensitive detector (PSD) [38]. Full-pattern refinement was carried out using *Topas* software, version 5.0[39], using structural models derived from previous research on BCZT, for cubic [40] and tetragonal [41] structures, and modified according to the compositions employed in the present work.

The sintered pellets were mounted and ground using 800, 1200 and 2500 grade SiC paper and then polished initially using 6, 1 and 0.25 micron diamond paste, followed by final polishing with dilute OPS (Oxide Polishing Suspension). Afterwards, they were chemically etched by immersing into a solution of (4% HCl +1% HF+ 95% distilled water) for 20 seconds. Microstructures of chemically-etched and carbon-coated surfaces of slow-cooled and quenched-poled samples were characterised by scanning electron microscopy (Philips XL30 FEG-SEM).

3 Results and discussion.

3.1 Structure and ferroelectric behaviour at room temperature

3.1.1 Crystal structure

The SXPD results obtained for 0.35BCZT-0.65KBT-2wt% Bi_2O_3 ceramics with x=0.06 and x=0.15 are shown in Figure 1. For both compositions, a perovskite structure is evident, indicating the formation of the solid solution between BCZT and $K_{0.5}Bi_{0.5}TiO_3$. The tolerance factor (t) was calculated as 0.9871 and 0.9835 for x=0.06 and x=0.15 ceramics, respectively. According to these results, it can be predicted that the tetragonal phase should be more stable in the former case. It is apparent that peak splitting occurs clearly in some grain families, such as $\{200\}_{pc}$, $\{211\}_{pc}$ and $\{220\}_{pc}$ (using the *pseudo-cubic* setting), particularly for the quenched and quenched-poled samples, indicating the presence of lower symmetry perovskite type phases.

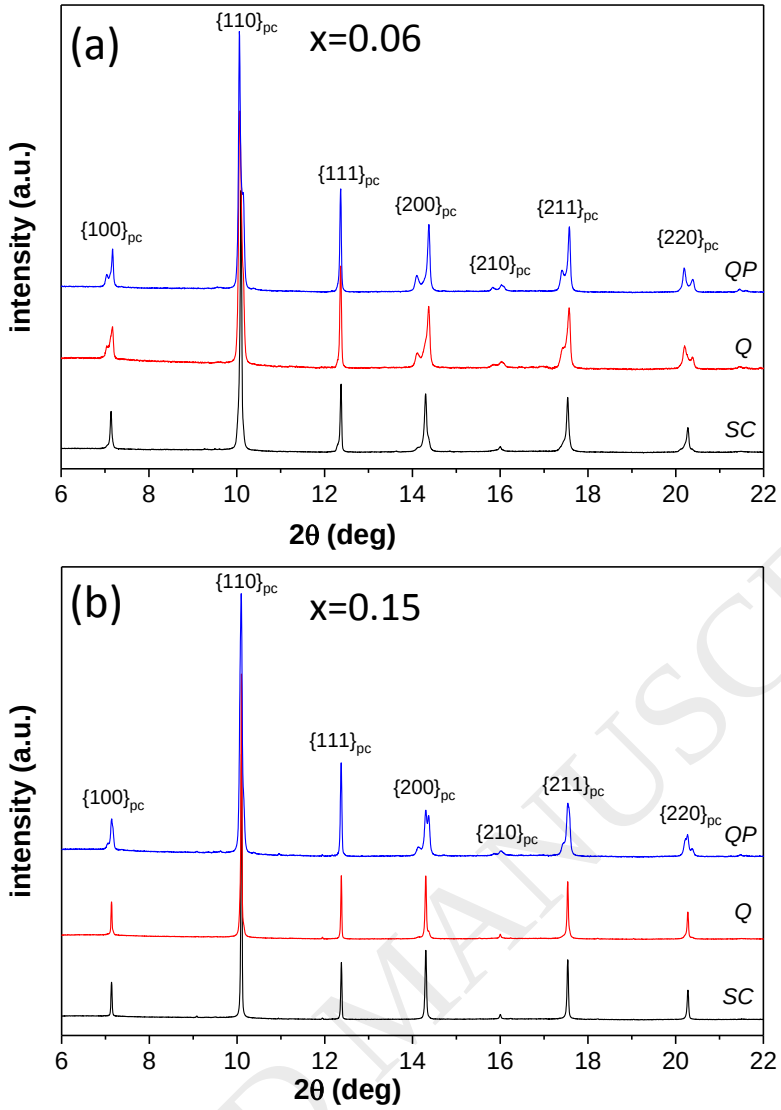

Figure 1. Room temperature SXPD patterns of BCZT-KBT ceramics; (a) *x*=0.06 and (b) *x*=0.15, in various states; slow-cooled (*SC*), quenched (*Q*) and quenched-poled (*QP*).

In order to determine the influence of quenching and poling on the crystal structure, full pattern fitting was carried out using P4mm tetragonal and $Pm\bar{3}m$ cubic structures. Figure 2 illustrates selected peak profiles showing the pseudo-cubic $\{111\}_{pc}$ and $\{200\}_{pc}$ reflections as characteristic split peaks. A summary of the crystallographic parameters determined from this analysis is given in Table 1.

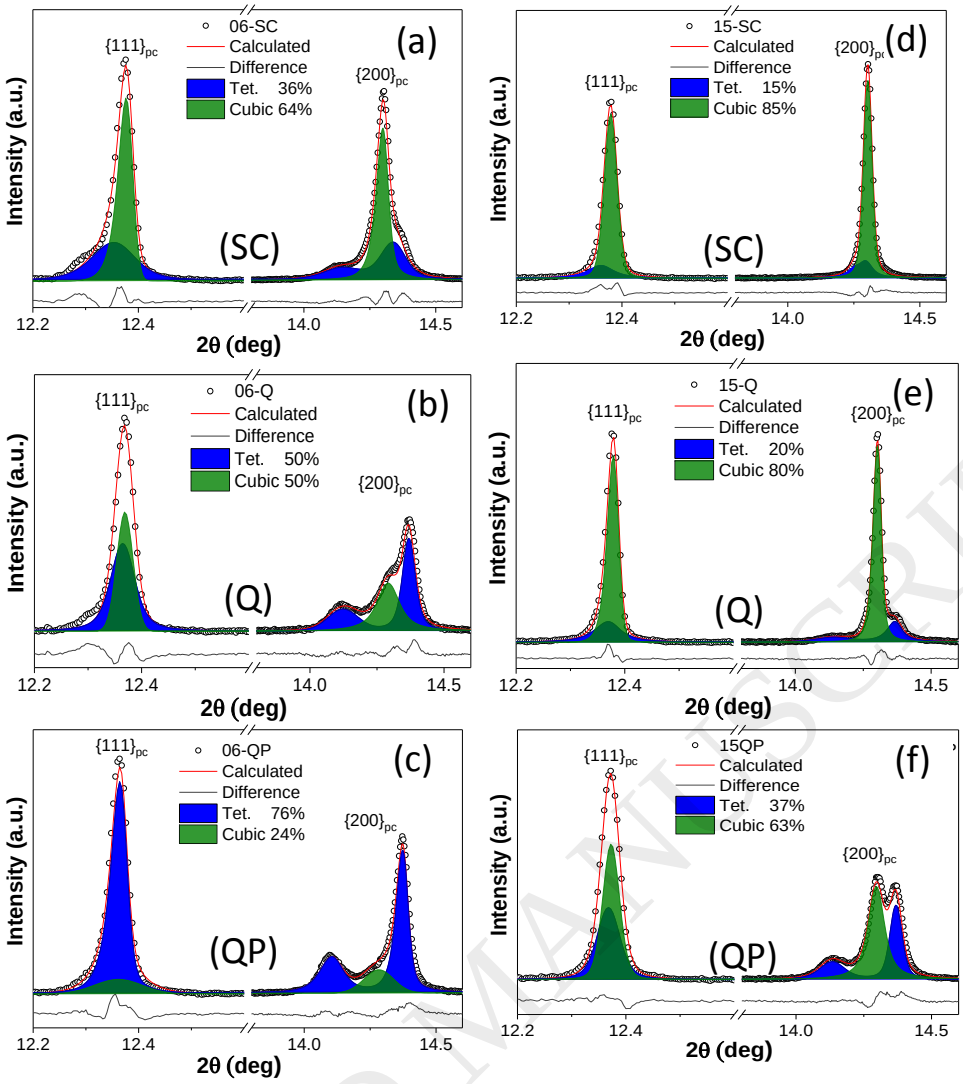

Figure 2. Experimental, calculated and difference data obtained by full pattern refinement of SXPD patterns showing $\{111\}_{pc}$ and $\{200\}_{pc}$ reflections of BCZT-KBT ceramics in various states; slow-cooled (*SC*), quenched (*Q*) and quenched-poled (*QP*) for (a)-(c) x=0.06 and (d)-(f) x=0.15.

Analysis of the diffraction patterns for the slow-cooled ceramics, presented in Figure 2 (a) and (d), indicates the coexistence of a tetragonal phase along with a dominant cubic phase. However, the occurrence of pronounced peak broadening for x=0.06 indicates a higher tetragonal phase fraction (36%) in comparison with the case for x=0.15 (15%). The identification of a high cubic phase fraction in the present study is consistent with previous reports of the solid solutions between BT- and Bi-based perovskites. For example, it was found that the incorporation of approximately 10 mol% of either $Bi(Mg_{0.5}Ti_{0.5})O_3$ or $Bi(Zn_{0.5}Ti_{0.5})O_3$ into $(Ba_{0.8}Ca_{0.2})TiO_3$ induced a structural transformation from tetragonal to pseudo-cubic [42, 43]. For the binary system, $(1-x)BaTiO_3–xBiScO_3$ (x=0.0-0.5), it was reported that the tetragonal distortion disappeared beyond 5 mol% $BiScO_3$, due to a change of structure from tetragonal to pseudocubic [24]. Interestingly, it was also observed that core-shell features occurred in the microstructure of ceramics with more than 3 mol% $BiScO_3$, resulting from difficulty of homogenisation during sintering.

It was also reported by Calisir [31] that the addition of 1 mol% MnO_2 into the calcined composition of $0.75BiFeO_3$–$0.25BaTiO_3$ induces structural and microstructural changes due to the emergence of a pseudo-cubic ($Pm\bar{3}m$) phase besides the rhombohedral (R3c) phase and chemical heterogeneity in the form of core–shell grain microstructures. The formation of such core–shell structures can be attributed to kinetic factors and differences in reactivity between the constituents during sintering; the phase formed first makes the core and that forming later constructs the shell. Alternatively, thermodynamic immiscibility between solid solution constituents is another important factor which could lead to further nanoscale segregation in the shell regions during slow cooling [31].

Table 1. Cubic and tetragonal coexisting phases, phase fractions, lattice parameters and GOF of BCZT-KBT ceramics with *x*=0.06 and *x*=0.15, at room temperature. Numeric values in parentheses denote the uncertainty in the last significant digit(s).

Composition	State	Phases present	Phase fraction (%)	Lattice parameter		$(c/a)_T$	GOF*
				a (Å)	c (Å)		
x=0.06	SC	T-C	T= 36.2(7) C= 63.8(7)	a_T=3.9562(03) a_C=3.9677(32)	c_T= 4.0102(03) -	1.0136	2.12
	Q	T-C	T= 49.6(7) C= 50.4(7)	a_T= 3.9509(02) a_C= 3.9720(31)	c_T= 4.0192(03) -	1.0173	1.85
	QP	T-C	T= 76.1(7) C= 23.9(7)	a_T= 3.9474(01) a_C= 3.9705(02)	c_T= 4.0215(01) -	1.0188	1.81
x=0.15	SC	T-C	T= 15.3(6) C= 84.7(6)	a_T= 3.9719(02) a_C= 3.9699(04)	c_T= 3.9840(02) -	1.0030	2.68
	Q	T-C	T= 19.6(6) C= 80.4(6)	a_T= 3.9506(03) a_C= 3.9686(06)	c_T= 4.0137(03) -	1.0160	2.08
	QP	T-C	T= 36.5(7) C= 63.5(7)	a_T= 3.9512(03) a_C= 3.9710(03)	c_T= 4.0166(03) -	1.0166	1.65
*Goodness of fit (GOF) is the value of R_{wp}/R_{exp}.							

After quenching, as shown in Figure 2 (b) and (e), clear splitting of the $\{200\}_{pc}$ peak was observed for the ceramic with *x*=0.06, which is associated with tetragonal distortion and an increase of the tetragonal phase fraction from 36% to 50%. The coexisting cubic phase is indicated by the central $\{200\}_{pc}$ cubic peak, as shown in Figure 2(b). In contrast, for the ceramic with *x*=0.15, there was little change after quenching, comparing Figure 2(d) and (e) with respect to enhancement of tetragonal phase indicated by the shoulders around the $\{200\}_{pc}$ peak. These observations suggest that the Ca and Zr contents of the BCZT component play an important role in controlling the stability of the ferroelectric tetragonal phase in the BCZT-KBT solid solution, both for slow-cooled and quenched samples. The effect of quenching on structural characteristics was observed previously in various perovskite-type solid solutions. Muramatsu [30] reported that the lattice distortion of the rhombohedral phase in lead free $(Bi_{0.5}Na_{0.5})TiO_3$ (BNT) ceramic was enhanced following the quenching process and was strongly dependent on the quench temperature. It was also reported by Lee [44] that the application of a quenching process for $0.67Bi_{1.05}FeO_3$-$0.33BaTiO_3$ ceramics, causes increases in all lattice parameters for both rhombohedral and tetragonal phases.

In related research, Kim [27] investigated the effects of annealing and quenching on ferroelectric properties and structural evolution of $0.80BiFeO_3$–$0.20BaTiO_3$ solid solutions to reveal the role of heat treatment in enhancement of their properties. The optimum results were achieved by quenching from 800 °C in water. It was observed

that a single, broad $\{110\}_{pc}$ peak in the slow-cooled sample became clearly split after quenching, indicating the presence of the rhombohedral structure. By examination of crystallographic parameters, an increasing A-O bond-length was observed due to rapid cooling, while the B-O bond-length was maintained in all the slow-cooled, annealed, and quenched samples. It was suggested that the relaxation of the lattice strain due to the heat treatment was the main cause of the significant enhancement in ferroelectric behaviour.

The application of an electric field up to 6 MV m^{-1} led to further changes in the diffraction peak profiles, as shown in Figure 2(c) and (f). It is evident that the intensity of the $\{200\}_{pc}$ cubic peak decreased further and the splitting of the $\{200\}_{pc}$ tetragonal peak became more clearly evident in both ceramics due to an increase of tetragonal phase fraction, from 50% to 76% for x=0.06 and from 20% to 37% for x=0.15. Similar effects of quenching and poling were observed by Su [45] in $0.75BiFeO_3$-$0.25BaTiO_3$ ceramics. It was reported that splitting of the $\{111\}_{pc}$ peak, associated with rhombohedral distortion, occurred after quenching and further changes in the relative peak intensities developed after poling due to ferroelectric domain switching. Furthermore, the slow-cooled sample in the present study showed a poorly developed domain structure, whereas a well-aligned ferroelectric domain pattern was clearly observed in the quenched sample. Similar domain reorientation effects cannot be observed in these SXPD results, due to the randomly-oriented nature of the particles in the crushed powder samples, but the improved stability of the ferroelectric phase as a result of the poling process is clearly evident.

3.1.2 Microstructure

The microstructures of the BCZT-KBT ceramics with x=0.06 and x=0.15 in slow-cooled and quenched-poled states are illustrated in Figure 3. The dominant feature in the slow-cooled samples is the core-shell type microstructure, as shown in Figure 3(a) and (c). The identification of core and shell regions in these ceramics was discussed in our previous investigation [20] in terms of tetragonal ferroelectric BCZT-rich cores with pseudo-cubic relaxor ferroelectric KBT-rich shell regions. On the other hand, clearly defined ferroelectric domain structures were observed throughout the grains in the quenched-poled sample with x=0.06, as shown in Figure 3(b). These features can also be seen in some grains for the ceramic with x=0.15, Figure 3(d).

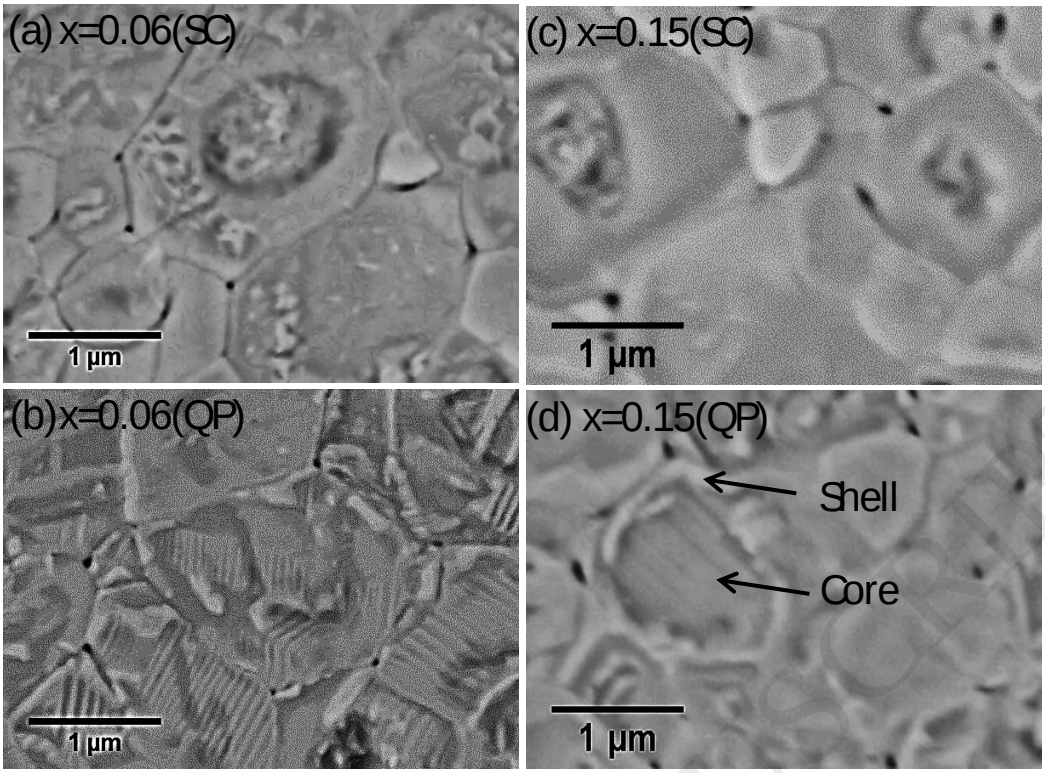

Figure 3. Backscattered electron (BSE) images of chemically-etched surfaces of BCZT-KBT ceramics in various states; slow-cooled (SC) and quenched-poled (QP) for (a)-(b) x=0.06; (c)-(d) x=0.15.

3.1.3 Ferroelectric properties

Figure 4 shows the P-E and J-E loops, measured at room temperature, of the slow-cooled and quenched states for both ceramics, with x=0.06 and 0.15. The slow-cooled sample with x=0.06, shown in Figure 4(a), has a slightly pinched P-E loop indicated by two peaks in the J-E curve with remanent polarisation, P_r, of 0.12 C m^{-2} and coercive field, E_c, of 1.9 MV m^{-1}. A slightly higher P_r of 0.14 C m^{-2} and substantially larger E_c of 3.7 MV m^{-1} was obtained for the corresponding quenched sample; these variations in properties are attributed to the higher proportion of the long-range ordered ferroelectric tetragonal phase in the quenched ceramic. For x=0.15, the influence of quenching on the P-E loops was even more dramatic; the loop of the slow-cooled sample with x=0.15 was slim and tilted with a very low P_r value of 0.04 C m^{-2}, while that of the quenched sample had a typical near-rectangular appearance with a P_r value of 0.18 C m^{-2}, as shown in Figure 4(b).

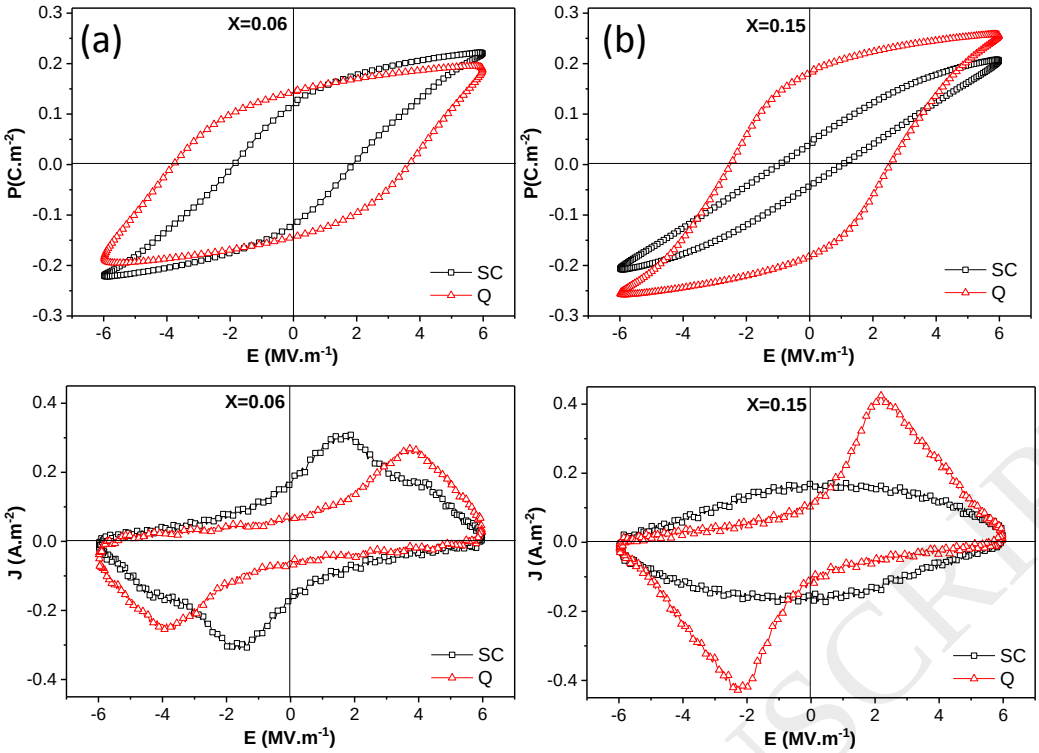

Figure 4. Room temperature P-E hysteresis loops of slow-cooled (*SC*) and quenched (*Q*) BCZT-KBT ceramics for (a) *x*=0.06 and (b) *x*=0.15.

The occurrence of such pinched, or slim, P-E loops is a result of restriction of ferroelectric domain switching, which might be attributed to several causes [46]. For instance, hindering of domain wall movement can occur due to domain wall pinning by oxygen vacancy-cation defect dipoles [47, 48], or to existence of antiferroelectric phases [14, 49]. In relaxor ferroelectrics, it could arise as a result of *ergodicity* phenomena, in which the transformation between PNRs and ordered ferroelectric domains exhibits complete or partial reversibility [12, 13]. Generally, the presence of polar nanoregions is a typical characteristic of relaxor ferroelectrics [2, 9]. Another reason could be related to the presence of core-shell type microstructures [31], in which two different solid solutions having different ferroelectric properties could exist such as in the $BiFeO_3$-$BaTiO_3$ system [50, 51] where rhombohedral ferroelectric $BiFeO_3$-rich cores with pseudo-cubic relaxor ferroelectric $BaTiO_3$-rich shell regions were observed. Two possible mechanisms to restrict domain switching in such materials were proposed by Calisir [31]. One possibility is that ferroelectric domain switching in the core could be constricted elastically by the nanodomain-structured shell, if it was relatively inactive. Alternatively, the electric field-induced phase transformation and domain switching in the shell region could be elastically constrained by a ferroelectric core having a high coercive field.

In this study, as mentioned in our previous work [20], the constricted P-E loops were attributed to the presence of reversible polarisation switching in PNRs in addition to the chemical heterogeneity that was observed in the form of core-shell grain structures, comprising tetragonal ferroelectric BCZT-rich cores with pseudo-cubic relaxor ferroelectric KBT-rich shell regions. Therefore, two factors could influence ferroelectric behaviour in this study, which are the ferroelectric phase fraction

(represented by the core) and the nature of PNRs within the shell (ergodic or nonergodic). Thus, for slow-cooled samples, the higher polarisation values for the ceramic with x=0.06, relative to that with x=0.15, are attributed firstly to the higher percentage of the tetragonal ferroelectric phase which was around 36 % compared with 15 %, as shown in Table 1. Secondly, since the shell regions contain PNRs with different responses under an electric field, we can propose that they are mostly irreversible PNRs (*non-ergodic* state) in the ceramic with x=0.06 and mostly reversible PNRs (*ergodic* state) in the ceramic with x=0.15.

On the other hand, after quenching the ceramic with x=0.06 has a more-rectangular P-E loop and higher coercive field. Furthermore, opening of the P-E loop was observed as can be seen in J-E curve, which exhibits two well-defined singular peaks that indicate polarisation reversal due to ferroelectric domain switching around a distinct coercive field. Also, the quenching process causes a dramatic increase in remanent polarisation and coercive field in the ceramic with x=0.15. These results indicate enhancement of domain switching in the quenched samples. Furthermore, the high values of coercive field in these samples, which are consistent with that of KBT, indicate that the shell region is the more active component in these materials, since the shell is KBT-rich.

3.1.4 Strain-electric field response

High field *x-E* loops of the slow-cooled and quenched states for both ceramics are illustrated in Figure 5. The results demonstrate the same trends as those observed in the *P-E* loops and are consistent with our interpretation of the structural changes induced by the quenching process. For x=0.06, shown in Figure 5(a), both slow-cooled and quenched ceramics exhibit x-E curves with a typical butterfly-type form showing substantial levels of hysteresis together with both positive and negative variations in strain relative to the remanent state. Maximum positive strains, x_{max}, of 0.144% and 0.068% were obtained at an electric field of 6.0 MV m^{-1} for the slow-cooled and quenched ceramics, respectively. It is also worth noting that the slow-cooled specimen has a lower coercive field in comparison with that of the quenched ceramic, in agreement with the P-E loops reported above. The high strain of the slow-cooled specimen is attributed to the presence of reversible PNRs (ergodic state) within the shell, whereas the lower x_{max} and high E_c for the quenched ceramic are consistent with typical ferroelectric behaviour, which results from transformation of *non-ergodic* regions (that developed after quenching) into the long-range ordered ferroelectric state.

On the other hand, for x=0.15, shown in Figure 5(b), only the quenched sample shows positive and negative strain variations in the *x-E* curve. For the slow-cooled sample, a predominantly quadratic but hysteretic *x-E* relationship was obtained, similar to those reported for NBT-BT-KNN ceramics [13]. However, both the slow-cooled and quenched ceramics exhibited similar x_{max} values of 0.12% and 0.13% respectively. These observations are consistent with the above explanation of reversible

polarisation switching due to the presence of PNRs in an ergodic state within the shell regions for the slow-cooled ceramic.

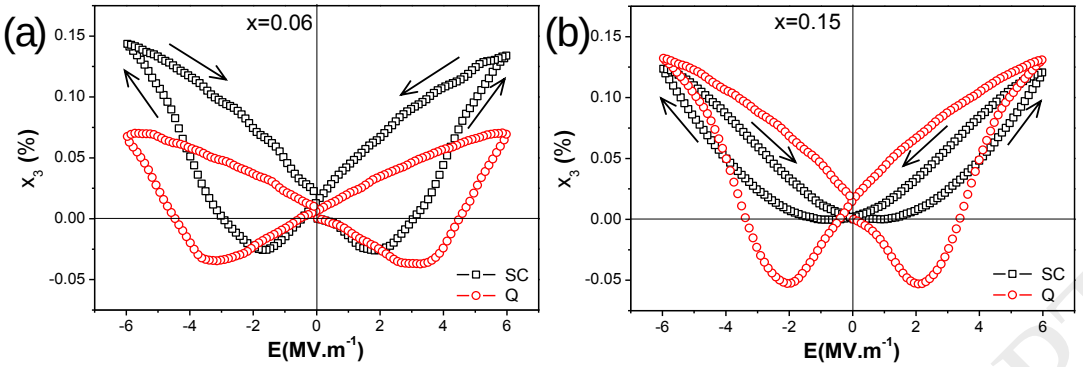

Figure 5. Room temperature strain-electric field loops of slow cooled (SC) and quenched (Q) BCZT-KBT ceramics for (a) x=0.06 and (b) x=0.15.

The same data is re-plotted in Figure 6 to demonstrate the relationships between strain and polarisation. *x-P* plots presented in Figure 6 (a) and (c) reveal a nearly parabolic response, which in the case of quenched samples is marked by some degree of hysteresis. Interestingly, no visible hysteresis of the strain with respect to the polarisation is observed for the slow-cooled x=0.15 sample, Figure 6(c), despite significant hysteresis in the x-E response as shown in Figure 5(b). Essentially, the strain closely follows a quadratic electrostrictive dependence on the polarisation. x-P^2 plots were constructed to calculate room-temperature electrostrictive coefficients, Q_{33}, as illustrated in Figure 6(b) and (d) for x=0.06 and x=0.15, respectively. It is worth noting that x is linearly proportional to P^2 and quenched ceramics exhibit slightly larger Q_{33} values than their slow-cooled counterparts, as listed in Table 2. Indeed, the quenched x=0.15 ceramics exhibit Q_{33} values as large as 0.035 m^4 C^{-2}, which according to recent literature [52] may be referred to as a *giant* electrostrictive coefficient, in comparison with conventional Pb-based ferroelectric relaxors, which exhibit Q_{33} in the order of 0.02 m^4 C^{-2}. In previous work, ultrahigh electrostrictive coefficients in Pb-free NBT-based ceramics have been observed near a thermotropic phase boundary, which is a thermally-induced boundary between two competing *ergodic* and *non-ergodic* relaxor phases [52]. This is consistent with a shell region encompassing *non-ergodic* PNRs embedded in an *ergodic* relaxor shell, as described in detail in the next section.

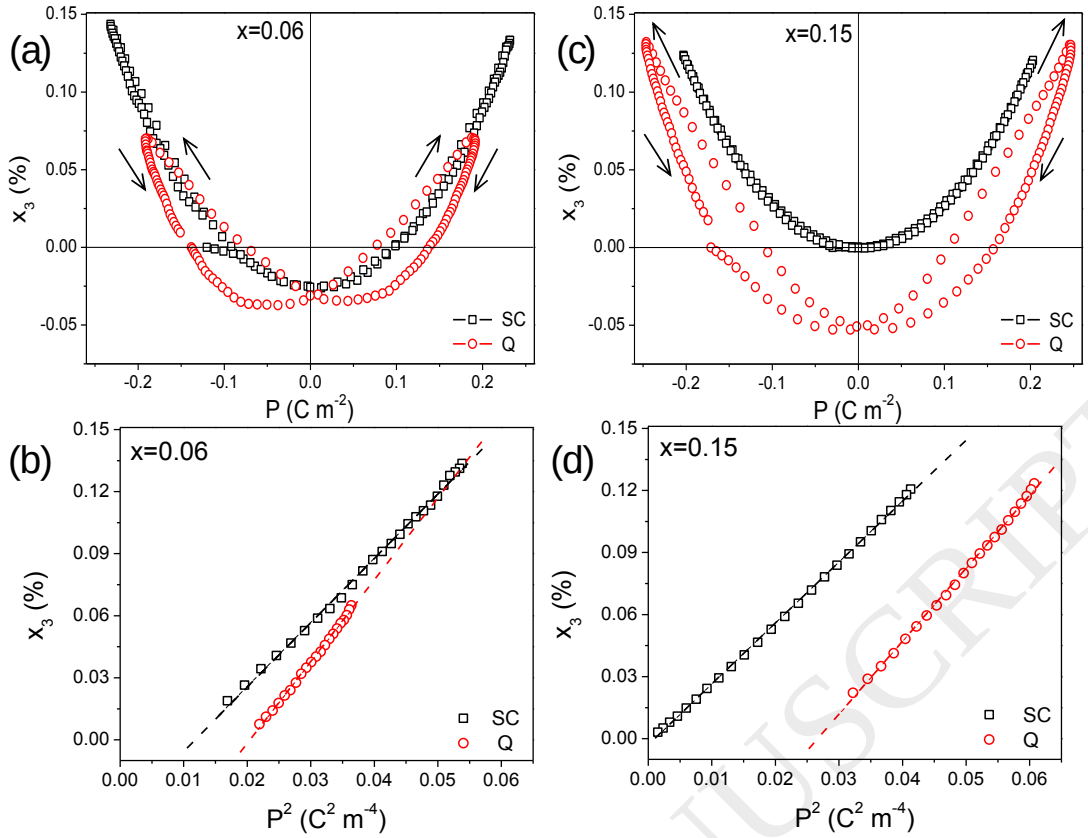

Figure 6. *x-P* and *x-P*^{2} relationships at room temperature of slow-cooled (SC) and quenched (Q) BCZT-KBT ceramics for (a-b) *x*=0.06 and (c-d) *x*=0.15.

Table 2. Comparison of the d_{33} and Q_{33} values for BCZT-KBT ceramics, with *x*=0.06 and 0.15, in slow-cooled and quenched states. The values of d_{33}* represent the *effective* high-field piezoelectric coefficient.

	x=0.06		*x*=0.15	
	SC	Q	SC	Q
d_{33} (pC N^{-1})	40	82	6.5	86
d_{33}^* (pm V^{-1}), x_{max}/E_{max}	240	113	202	220
Q_{33} (m^4 C^{-2})	0.031	0.04	0.03	0.035

3.1.5 Proposed model of quenching effect

In the present work, our explanation of the quenching effect on structure and ferroelectric properties is based on improvements in compositional homogeneity, leading to the formation of *non-ergodic* PNRs within the *ergodic* relaxor shell. To clarify this concept, a schematic representation of the evolution of PNRs within the shell regions after quenching and under application of an electric field is proposed for the ceramics with *x*=0.06 and 0.15, shown in Figure 7(a) and (b) respectively. These schematic diagrams are based on the observations of crystal structure, microstructure and ferroelectric properties described above.

For slow-cooled samples, the presence of larger ferroelectric core regions in the ceramic with *x*=0.06 is supported by the higher fraction of tetragonal phase as shown in the SXPD results, whereas the existence of *non-ergodic* PNRs within the *ergodic* relaxor shell is indicated by observations of well-saturated P-E loops and a well-defined switching field. On the other hand, for quenched samples, it is proposed that the quenching process induces the formation of *non-ergodic* regions within the *ergodic* relaxor shell, supported by an increase of the tetragonal phase fraction in both ceramics after quenching, as shown by the SXPD results shown in Figure 2(b) and (e). This improvement is attributed to enhancement of compositional homogeneity by retention of the chemically homogenous high temperature state. In contrast, we suppose that the slow-cooled samples are characterised by the development of nanoscale compositional heterogeneity in the shell regions as a result of immiscibility, giving rise to the formation of PNRs having an *ergodic* nature.

The last two sketches illustrate the effect of poling on the quenched samples. Based on the further increase of tetragonal phase content in both ceramics, from SXPD results and the dramatic enhancement of ferroelectric switching in the quenched samples, it is proposed that *non-ergodic* PNRs (developed after quenching) transform into the long-range ordered ferroelectric state. However, the higher cubic phase fraction, together with a slightly pinched P-E loop, for the quenched-poled sample with *x*=0.15 indicates that the fraction of *ergodic* PNRs is higher than that for *x*=0.06.

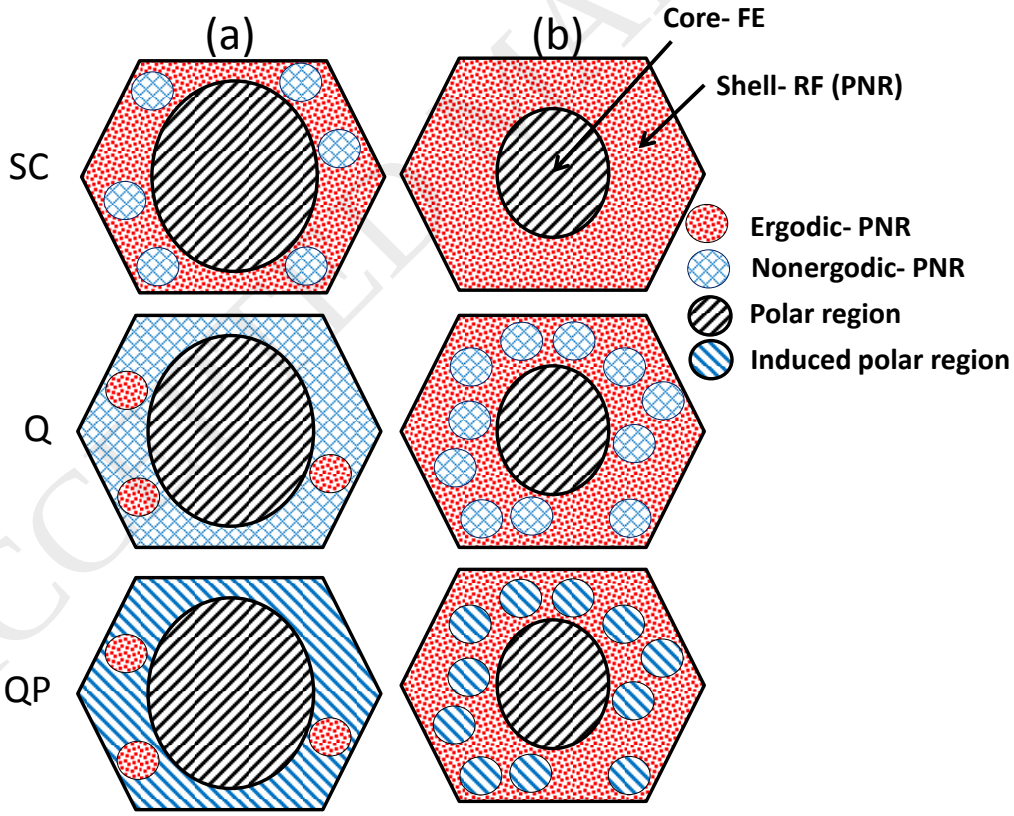

Figure 7. Schematic representation of the core–shell evolution after quenching and after application of an electric field for BCZT-KBT ceramics with (a) *x*=0.06 and (b) *x*=0.15.

From the above observations, it is evident that the ceramic with x=0.06 (lower percentage of Ca and Zr dopants) exhibits a more stable ferroelectric tetragonal phase

in the slow-cooled state. Furthermore, it exhibited more pronounced responses to the quenching and poling process, where further stabilisation of the ferroelectric tetragonal phase was obtained. Therefore, we can conclude that the stoichiometry of the BCZT component plays an important role in ferroelectric phase stabilisation.

3.2 Temperature-dependent variations in structure and properties

3.2.1 Crystal structure

The results of temperature-dependent in-situ SXPD measurements for BCZT-KBT powders in both quenched and quenched-poled states are illustrated in Figure 8 in terms of the evolution of $\{200\}_{pc}$ peak profiles over the temperature range 20 to 200 °C, using an Oxford Cryosystems 700 plus series liquid nitrogen cryostream. Whole-pattern fitting was carried out over a range of different temperatures, represented by the fitted profiles at 120 °C and 200 °C, illustrated in Figure 9.

The coexistence of tetragonal and cubic phases at room temperature was confirmed for both compositions, in quenched and quenched-poled states, as illustrated above in section 3.1.1. The relative fraction of each phase evolved during heating, as shown in Figure 10. For the quenched sample with x=0.06, the tetragonal phase content, determined as approximately 50 % at RT, decreased to 44% and 23% at around 120 and 200 ºC, respectively. Also, in the quenched-poled state, the field-induced tetragonal phase fraction of 76% at RT slightly decreased to 72 % at 120 ºC, then gradually to 45 % at 200 ºC. On the other hand, for the quenched sample with x=0.15, the predominant cubic phase content of 80 % at RT remained stable up to 120 ºC, then increased to 92 % at 200 ºC. Furthermore, the field-induced tetragonal phase fraction of 37 % at RT, in the quenched-poled state, remained stable up to 100 ºC, then decreased gradually to 22 % and 13 % at around 120 and 200 ºC, respectively. A summary of the phase fractions and lattice parameters determined from this analysis is provided in the Electronic Supplementary Information.

In view of the results presented in Figure 10, it is anticipated that the field-induced ferroelectric phase for the quenched ceramic with x=0.06 should remain stable during heating up to ~140 °C, Figure 10 (b), and up to ~100 °C for x=0.15, Figure **10**(d). Therefore, the thermally-induced structural transformations could influence the temperature-dependent dielectric and ferroelectric properties of quenched and quenched-poled ceramics, as shown below in Figure 11 and Figure 12.

For the quenched sample with x=0.06, presented in Figure 8 (a), it is evident that the $\{200\}_c$ peak develops progressively during heating due to the gradual transformation from tetragonal to cubic structure. The gradual growth in the cubic phase fraction is shown in Figure 10 (a), increasing from 50% (at RT) to 77% (at 200 °C). However, for the quenched-poled state, shown in Figure 8(b), the clear splitting of the $\{200\}_{pc}$ peak at RT after AC poling indicates the field-induced cubic-tetragonal phase transformation, resulting from the *non-ergodic* nature of the PNRs after quenching. Thus, the tetragonal phase is dominant with a phase fraction around 76%, which remains stable up to 140 °C then decreases gradually to 55% at 190 °C; this confirms

the stability of the *non-ergodic* behaviour up to 140 °C as demonstrated by the P-E loops during heating, as shown in Figure 12(b) below. Consequently, the cubic phase is dominant at 200 °C, as shown in Figure 10 (b). The structural transformations from tetragonal to cubic in both quenched and quenched-poled states for x=0.06 were incomplete at 200 °C.

In comparison, for the quenched sample with x=0.15, Figure 8 (c), at low temperatures there is a sharp $\{200\}_{pc}$ peak with high intensity at RT in addition to a shoulder on the right side, which is attributed to the $(200)_T$ peak. This indicates the dominance of the cubic phase, even room temperature. After poling, as shown in Figure 8(d), $(002)_T/(200)_T$ peaks are present beside the $\{200\}_{pc}$ peak, which indicates that the electric field-induced phase transformation occurred due to the presence of *non-ergodic* PNRs after quenching. During heating, this field-induced ferroelectric tetragonal phase remained stable up to ~100 °C at which its fraction was around 33%. Beyond this temperature, it decreased gradually, as shown in Figure 10 (d) due to the emergence of the *ergodic* state during heating, associated with the transformation to the pseudo-cubic relaxor ferroelectric phase. This behaviour is consistent with the presence of an inflection in the ε_r-T measurements at ~100 °C, Figure 11 (f).

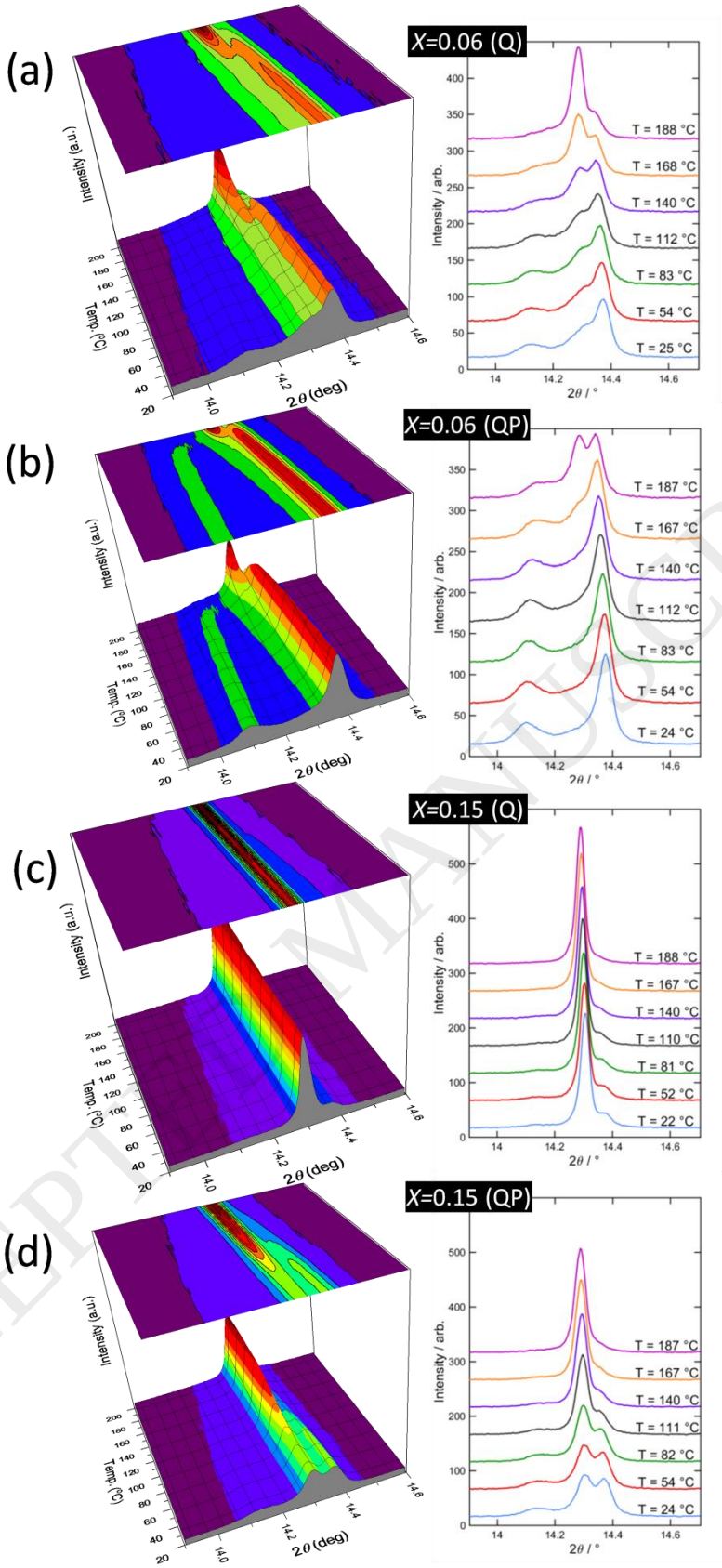

Figure 8. Evolution of $\{200\}_{pc}$ diffraction peak profiles for quenched (Q) and quenched-Poled (QP) BCZT-KBT powders as a function of temperature for (a)-(b) x=0.06, (c)-(d) x=0.15.

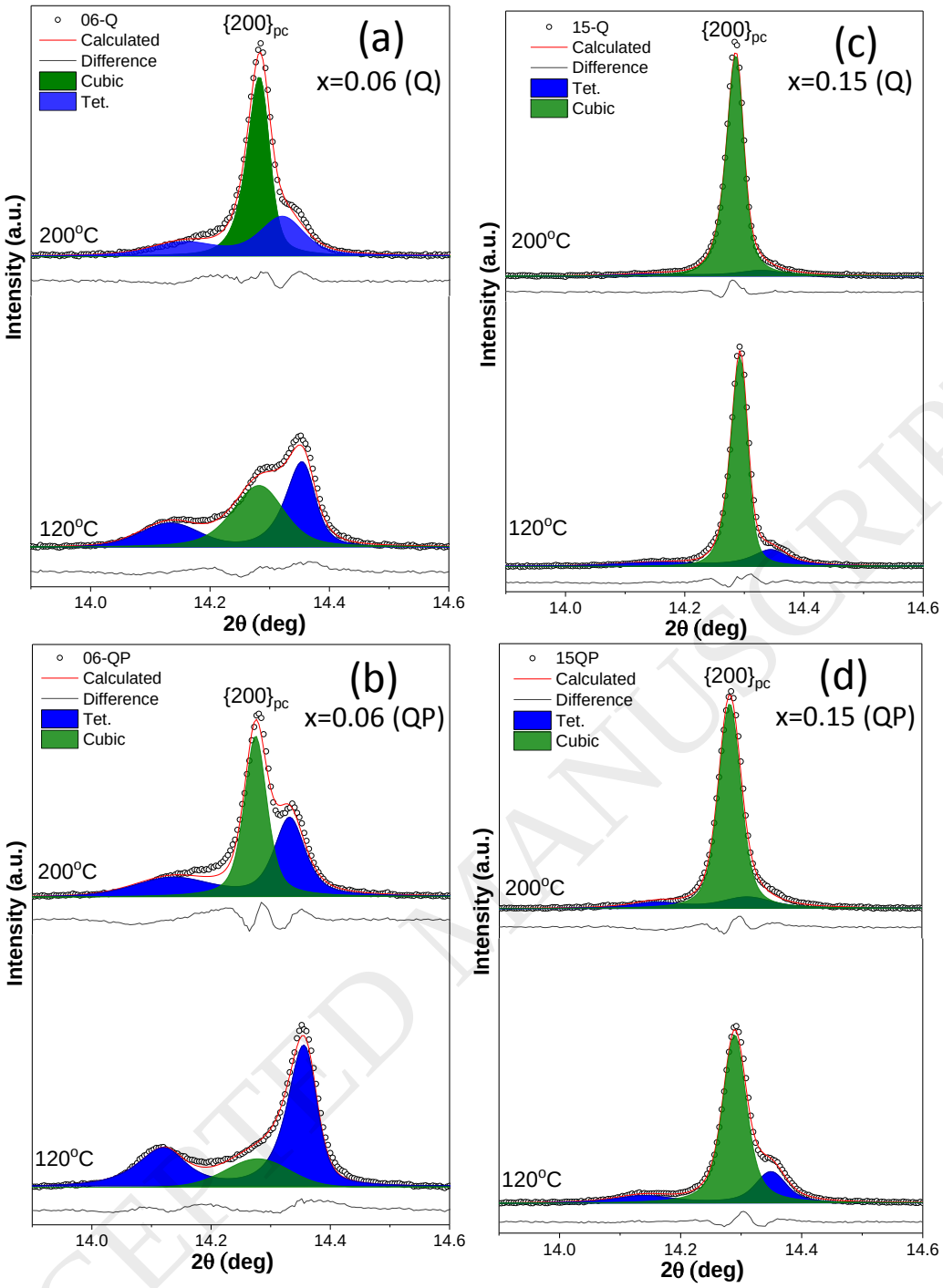

Figure 9. The experimental, calculated and difference data obtained by full pattern refinements showing $\{200\}_{pc}$ diffraction peak profiles for quenched (Q) and quenched-Poled (QP) BCZT-KBT powders at temperatures of 120ºC and 200ºC for (a)-(b) x=0.06, (c)-(d) x=0.15.

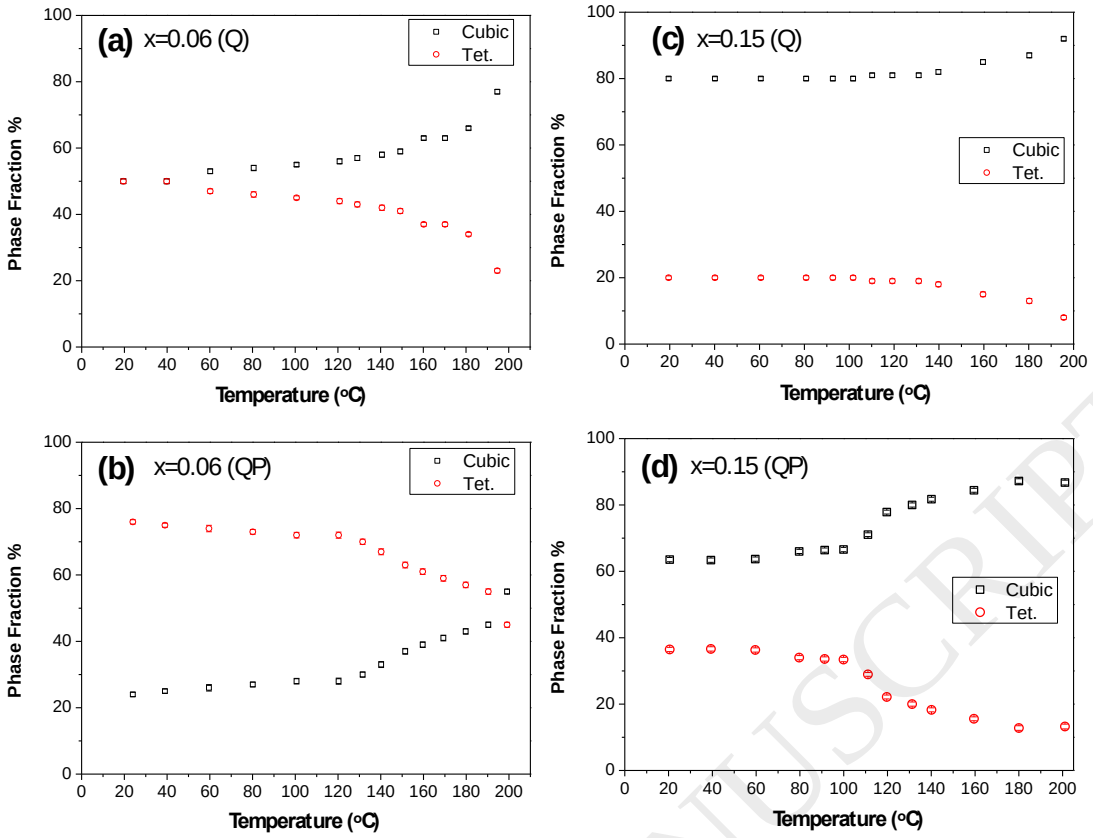

Figure 10. Evolution of phase fractions for quenched (Q) and quenched-poled (QP) BCZT-KBT powders as a function of temperature for (a)-(b) x=0.06, (c)-(d) x=0.15. Note that error bars are smaller than symbol size.

3.2.2 Dielectric permittivity

The temperature-dependent dielectric properties of the BCZT-KBT ceramics in various states are shown in Figure 11. The ε_r-T curves of slow-cooled specimens for both compositions exhibit classic frequency-dispersive relaxor behaviour having one broad peak at a maximum temperature T_m ~250 ºC and ~200 ºC at 100 kHz for *x*=0.06 and *x*=0.15, respectively, as shown in Figure 11(a) and (d). However, the slow-cooled sample with *x*=0.15 exhibits more diffuse and dispersive behaviour than that for *x*=0.06. After quenching, two peaks were observed in the ε_r-T curves at ~210 ºC and ~300 ºC, which are tentatively attributed to separate transitions in the shell and core regions respectively [31]. The ε_r-T and tanδ-T relationships presented in Figure 11 (c) and (f) illustrate the effects of poling on the quenched samples. For *x*=0.06, a reduced frequency dependence was observed up to ~200 ºC, whereas, for *x*=0.15 an additional anomaly was observed at ~100 ºC, which is associated with the depolarisation temperature, as shown below in section 3.2.5.

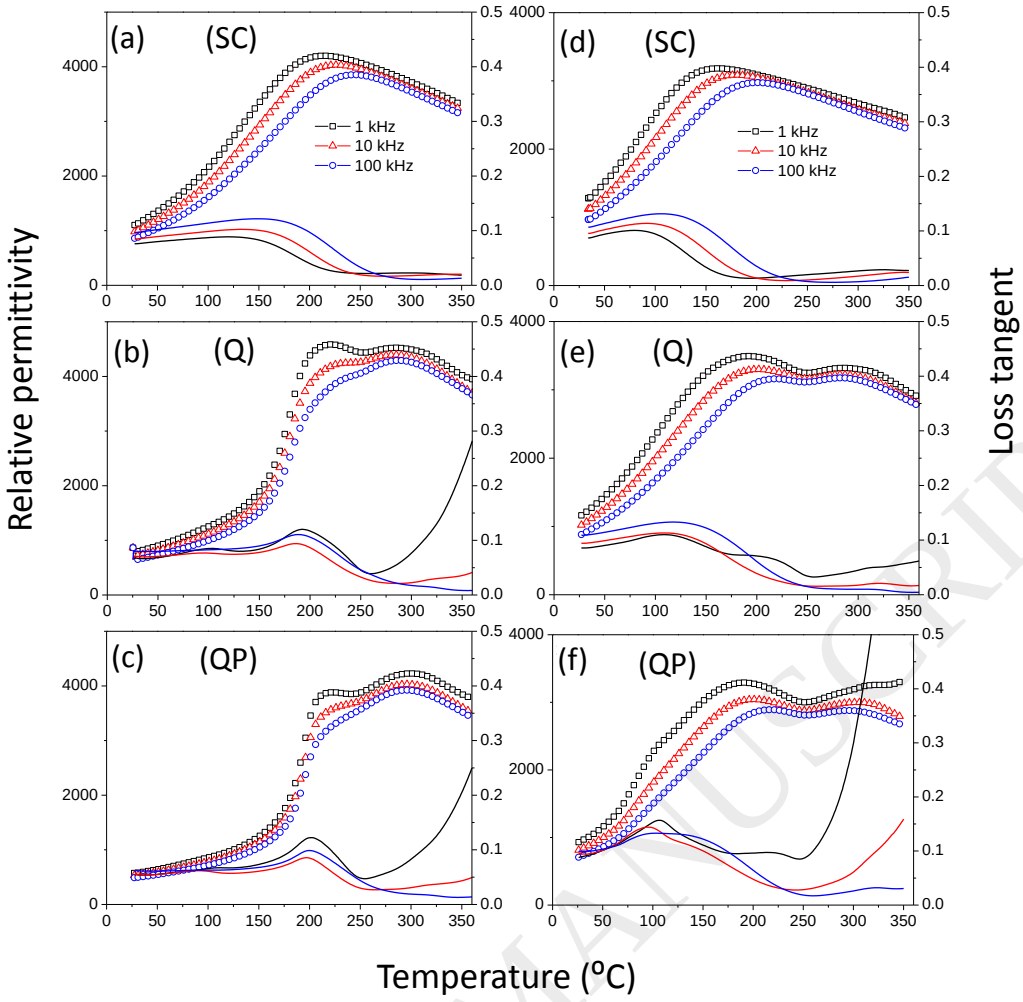

Figure 11. Temperature-dependence of dielectric permittivity and loss of BCZT-KBT ceramics in various states; slow-cooled (*SC*), quenched (*Q*) and quenched-poled (*QP*) for (a)-(c) *x*=0.06 and (d)-(f) *x*=0.15.

3.2.3 Ferroelectric hysteresis

The influence of heating on the ferroelectric properties of the slow-cooled and quenched samples is illustrated by the results presented in Figure 12. It is evident that progressive constriction occurs in the P-E loops of slow-cooled samples upon heating which indicates the development of a reversible electric field-induced transformation from nanopolar to long-range ordered ferroelectric state, as shown in Figure 12(a) and (c). On the other hand, for the quenched samples this behaviour was observed only in the ceramic with x=0.15. In contrast, the ferroelectric switching characteristics for x=0.06 were enhanced with increasing temperature, with both the remanent and saturation polarisation values increasing due to reduction of the coercive field and enhancement of domain switching behaviour.

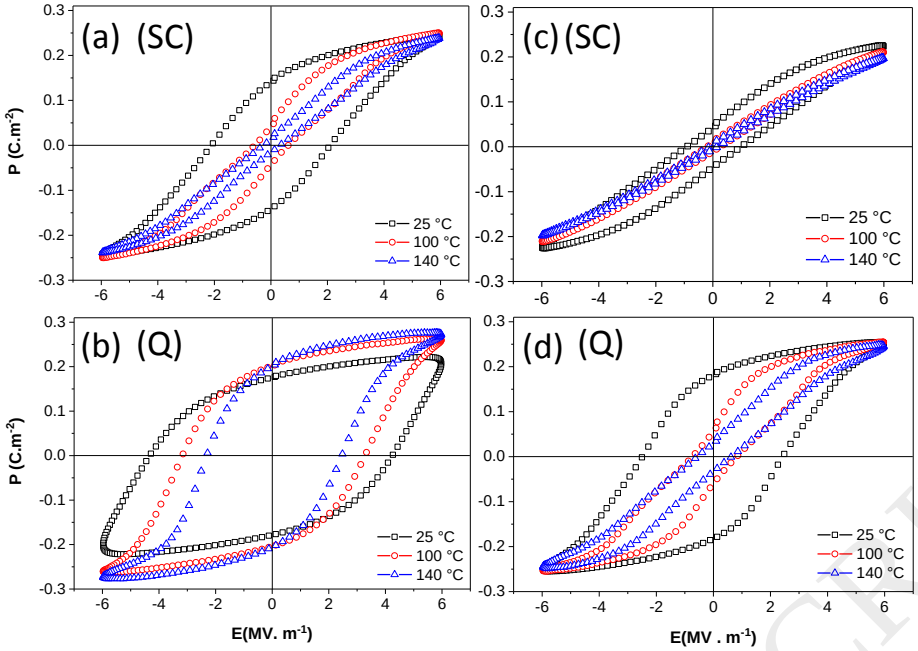

Figure 12. P-E loops of slow-cooled (SC) and quenched (Q) BCZT-KBT ceramics (a)-(b) x=0.06, (c)-(d) x=0.15 at different temperatures.

3.2.4 Strain-electric field response

In-situ S-E loops for quenched BCZT-KBT, acquired in the 20 to 140 °C temperature range, are illustrated in Figure 13. For x=0.06, the coercive field decreases and the maximum achievable strain increases with increasing temperature. This again supports an enhancement of domain switching with increasing temperature. A slight decrease in the negative strain with increasing temperature can be ascribed to a concomitant decrease in the tetragonal phase, as shown in Figure 10(a). On the other hand, the variations in the S-E relationship for x=0.15 are remarkably different; with increasing temperature the ferroelectric-like response is gradually reduced and at 100°C is replaced by a largely reversible *ergodic* relaxor-type response with reduced hysteresis due to the significant decrease in the tetragonal phase content.

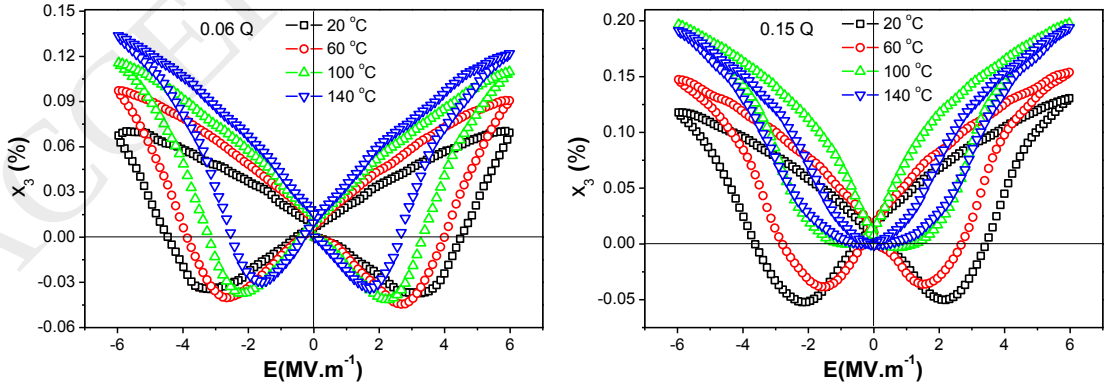

Figure 13. Temperature-dependence of strain-electric field loops for quenched BCZT-KBT ceramics with (a) *x*=0.06 and (b) *x*=0.15.

Nevertheless, the large strain and the constricted appearance of the P-E loops, Figure 12(d), is consistent with emergence of the *ergodic* state during heating, which is accompanied by a transformation to the pseudo-cubic relaxor ferroelectric phase. The aforementioned is corroborated by the *x*-*P* plots given in Figure 13. For x=0.15, the degree of hysteresis in the *x*-*P* curves slightly decreases, as shown in Figure 13(b). Furthermore, the maximum polarisation shows little temperature- dependence whereas the strain changes dramatically. In contrast, the results for x=0.06 show significant variations in both the maximum polarisation and strain with temperature. Consequently, this has an impact on the temperature-dependence of the electrostrictive coefficients, determined using data extracted from the *x*-P^2 relationships plotted in Figure 14. Indeed, Q_{33} for x=0.06 exhibits enhanced temperature stability in comparison with the case for x=0.15, as summarised in Figure **15**(a).

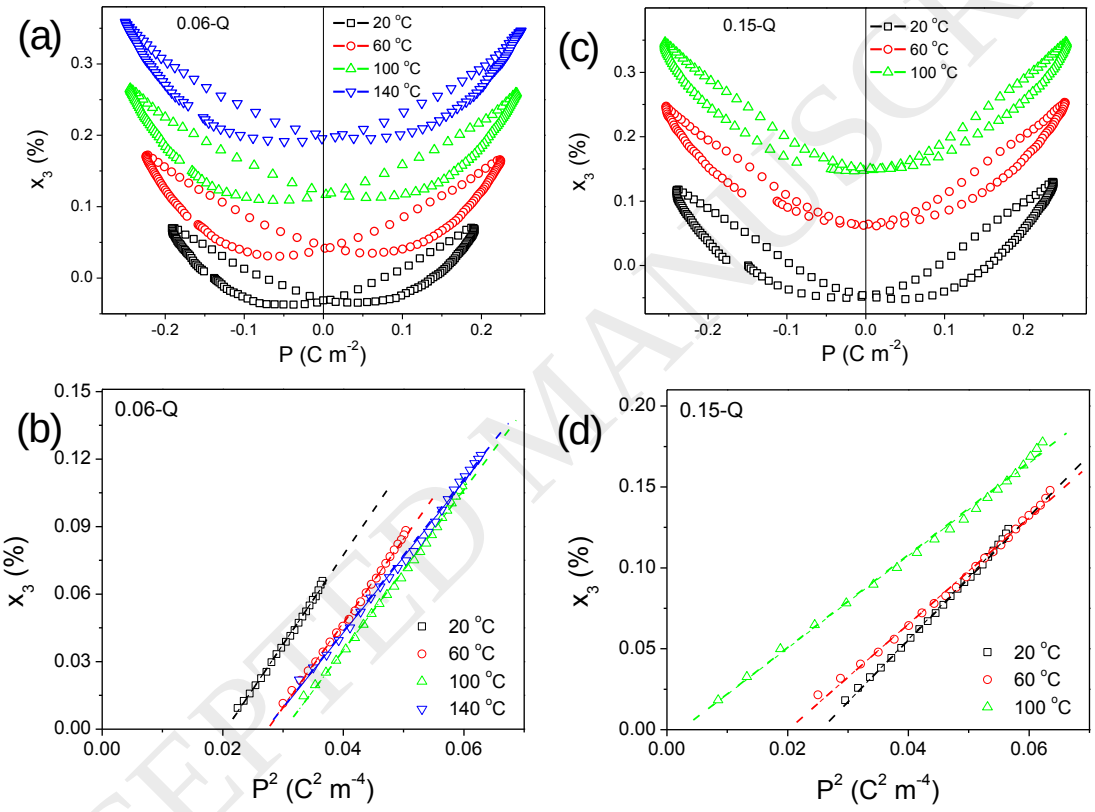

Figure 14. Temperature-dependence of *x*-*P* and *x*-P^2 relationships for quenched BCZT-KBT ceramics with (a-b) x=0.06 and (c-d) x=0.15. Note that the x_3 values in (a) and (c) are offset vertically by an arbitrary amount for clarity.

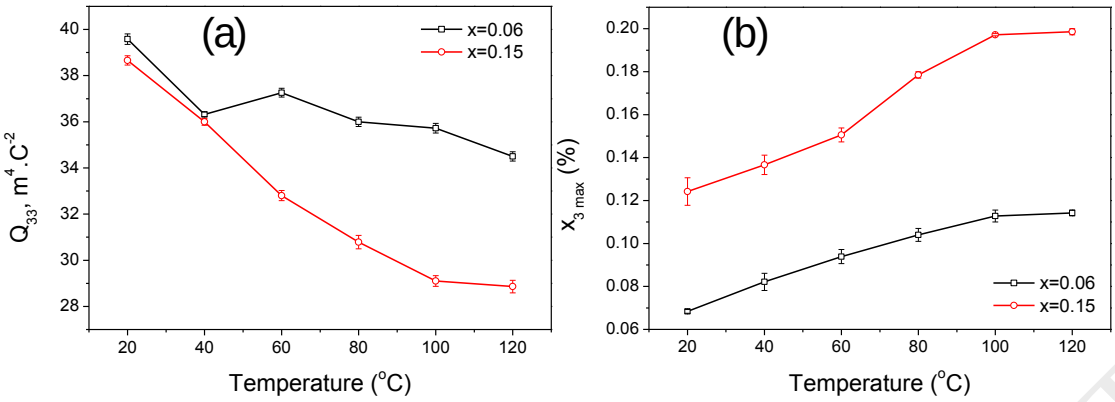

Figure 15. Temperature-dependence of (a) electrostrictive coefficient and (b) maximum strain of quenched BCZT-KBT ceramics for *x*=0.06 and *x*=0.15.

3.2.5 Thermal depolarization

The thermally-induced depolarisation results for both *x*=0.06 and 0.15 in the slow-cooled and quenched states are shown in Figure 16 in terms of the temperature-dependence of remanent polarisation and the depolarisation current density. The samples were poled in a silicone oil bath at room temperature by applying an AC field with amplitude 6.0 MV m^{-1} prior to the measurement. In general, the temperature at which the remnant polarization decreases rapidly is defined as the depolarization temperature, T_d, which can be identified most accurately from the peak in the J_d-T curve of the poled samples [36]. It is evident that the quenching process increased T_d from ~100ºC to ~160ºC for the BCZT-KBTceramic with *x*=0.06. In comparison, for x=0.15 the T_d of the quenched sample was ~60 ºC, while it was almost non-existent for the slow-cooled sample. These observations are consistent with those of the phase transformations identified by SXPD due to the close correlation between the emergence of cubic phase and depolarisation during heating.

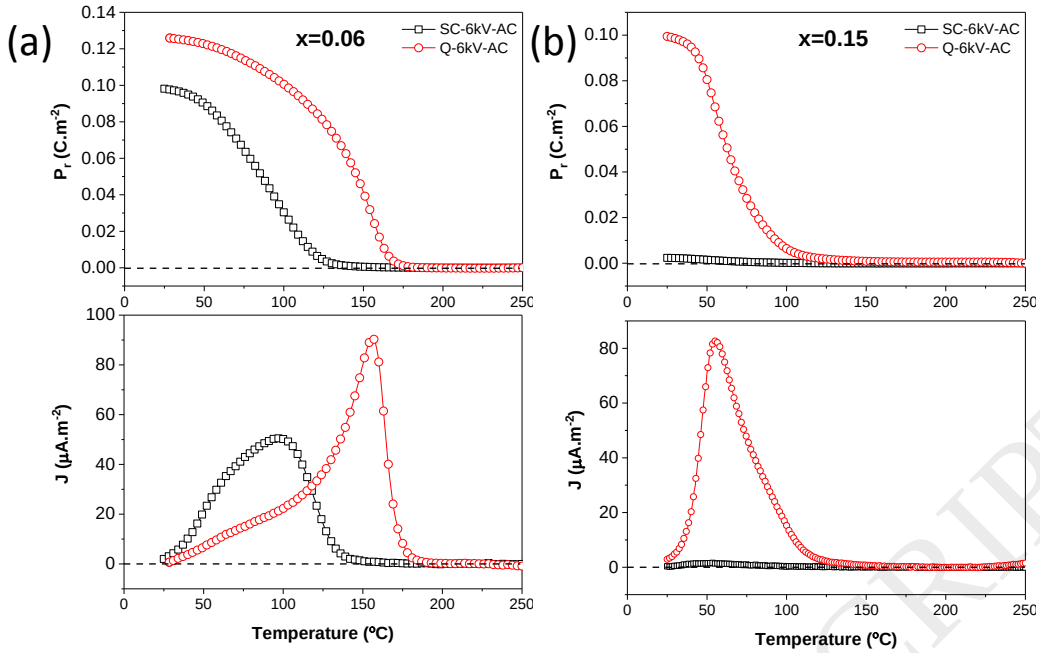

Figure 16. Thermal depolarization results for slow-cooled (SC) and quenched (Q) BCZT-KBT ceramics for (a) x=0.06 and (b) x=0.15.

In order to investigate the influence of the poling procedures, the quenched ceramic with *x*=0.06 was poled at room temperature using a DC electric field of 6.0 MV m^{-1}, for 5 min. Subsequently, the thermal depolarisation behaviour was measured, as shown in Figure 17. It is evident that both P_r and T_d were enhanced for the DC-poled ceramic, yielding enhancements in P_r, from 0.13 to 0.22 C m^{-2}, and T_d, from 160 to 190 °C.

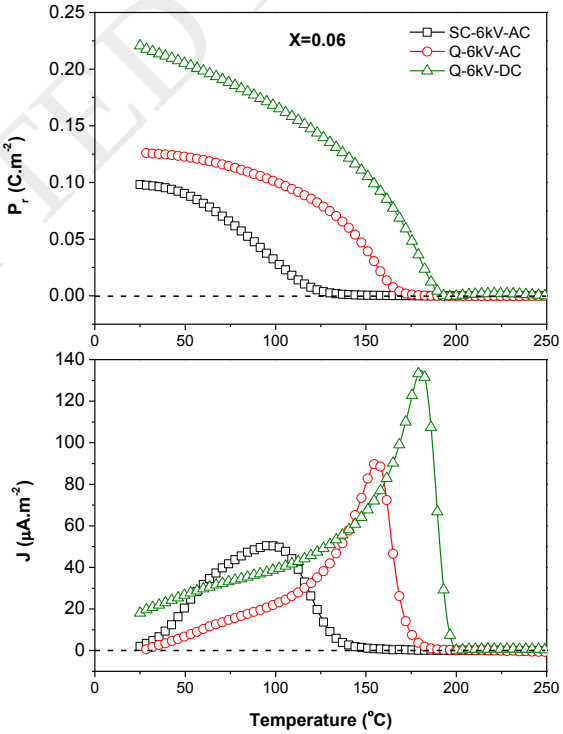

Figure 17. Influence of poling method on thermal depolarization behaviour for slow-cooled (SC) and quenched (Q) BCZT-KBT ceramic with x=0.06.

4 Conclusions

The structure and dielectric/ferroelectric properties of 0.35BCZT-0.65KBT ceramics with x=0.06 and 0.15, in the slow-cooled, quenched and quenched-poled states were investigated at RT and during heating. Chemical heterogeneity was observed in the form of core-shell grain microstructures, with emphasis on the presence of PNRs in the relaxor ferroelectric shell regions. Evaluation of the structure-property relationships demonstrated that the quenching process induces a transformation to long-range ordered ferroelectric domains and the formation of *nonergodic* PNRs within the *ergodic* relaxor ferroelectric shell, which transform irreversibly into the long-range ordered tetragonal ferroelectric phase after poling.

It is proposed that ferroelectric ordering in the shell regions is enhanced in the quenched state, relative to that of the slow-cooled state, due to the retention of the more chemically-homogeneous high temperature state by the quenching process. However, the field-induced ferroelectric state transformed back to the relaxor-like behaviour during heating in accordance with a gradual structural transformation from tetragonal to pseudocubic structure, which was confirmed by temperature-dependent in-situ SXPD measurements. A good correlation was established between structural evolution and the results of temperature-dependent dielectric, ferroelectric, and depolarization measurements. Generally, it was demonstrated that the lower percentage of Ca and Zr dopants (represented by the ceramic with x=0.06) stabilises the ferroelectric tetragonal phase in slow-cooled samples. Furthermore, the electric field-induced ferroelectric state for x=0.06 is more stable during heating than that for x=0.15. However, further research is necessary in order to improve fundamental understanding of the mechanism(s) responsible for the improvement of properties in BCZT-KBT ceramics due to quenching.

Acknowledgements:

The authors would like to thank Diamond Light Source, UK for access to beamline I11 (proposal number EE17673). The contribution of Ilkan Calisir (University of Manchester) through productive discussions is gratefully acknowledged. M. Al-Aaraji also thanks the Iraqi Ministry of Higher Education and Scientific Research (MOHESR), University of Babylon for financial support throughout his PhD programme.

5 References

[1] R.A. Cowley, S.N. Gvasaliya, S.G. Lushnikov, B. Roessli, G.M. Rotaru, Relaxing with relaxors: a review of relaxor ferroelectrics, Advances in Physics 60(2) (2011) 229-327.

[2] C. Bharti, A. Dutta, T.P. Sinha, Structural and Ferroelectric Properties of Complex Perovskites $Pb_{(1-x)}Ba_x(Fe_{1/2}Ta_{1/2})O_3$(x = 0.00, 0.05, 0.1, 0.15), Ferroelectrics 392(1) (2009) 20-32.

[3] K. Hirota, Phase Transitions in Relaxor Ferroelectricity, Ferroelectrics 354(1) (2007) 136-144.

[4] P.B. Jamieson, S.C. Abrahams, J.L. Bernstein, Ferroelectric Tungsten Bronze-type crystal structures. II. Barium Sodium Niobate $Ba_{(4+x)}Na_{(2-2x)}Nb_{10}O_{30}$, The Journal of Chemical Physics 50(10) (1969) 4352-4363.

[5] Z.G. Ye, Relaxor Ferroelectric Complex Perovskites: Structure, Properties and Phase Transitions, Key Engineering Materials 155-156 (1998) 81-122.

[6] V.A.I. G. A. Smolenskii, A. I. Agranovskaya, and S. N. Popov., Ferroelectrics with Diffuse Phase Transition, Soviet Physics-Solid State 2(11) (1961) 2584–2594.

[7] T.R. Shrout, S.J. Zhang, Lead-free piezoelectric ceramics: alternatives for PZT?, Journal of Electroceramics 19(1) (2007) 113-126.

[8] J. Rödel, K.G. Webber, R. Dittmer, W. Jo, M. Kimura, D. Damjanovic, Transferring lead-free piezoelectric ceramics into application, Journal of the European Ceramic Society 35(6) (2015) 1659-1681.

[9] M. Paściak, T.R. Welberry, J. Kulda, M. Kempa, J. Hlinka, Polar nanoregions and diffuse scattering in the relaxor ferroelectric $PbMg_{1/3}Nb_{2/3}O_3$, Physical Review B 85(22) (2012).

[10] V.V. Shvartsman, D.C. Lupascu, Lead-Free Relaxor Ferroelectrics, Journal of the American Ceramic Society 95(1) (2012) 1-26.

[11] R. Dittmer, Lead-free piezoceramics –ergodic and nonergodic relaxor ferroelectrics based on bismuth sodium titanate, PhD Thesis, University of Darmstadt, 2013.

[12] D.I. Woodward, R. Dittmer, W. Jo, D. Walker, D.S. Keeble, M.W. Dale, J. Rödel, P.A. Thomas, Investigation of the depolarisation transition in Bi-based relaxor ferroelectrics, Journal of Applied Physics 115(11) (2014) 114109.

[13] W. Jo, R. Dittmer, M. Acosta, J. Zang, C. Groh, E. Sapper, K. Wang, J. Rödel, Giant electric-field-induced strains in lead-free ceramics for actuator applications – status and perspective, Journal of Electroceramics 29(1) (2012) 71-93.

[14] J.-H. Cho, J.-S. Park, S.-W. Kim, Y.-H. Jeong, J.-S. Yun, W.-I. Park, Y.-W. Hong, J.-H. Paik, Ferroelectric properties and core shell domain structures of Fe-modified $0.77Bi_{0.5}Na_{0.5}TiO_3$ -$0.23SrTiO_3$ ceramics, Journal of the European Ceramic Society 37(10) (2017) 3313-3318.

[15] J.-H. Cho, C.-J. Jeon, K.-T. Lee, J.-S. Park, Y.-H. Jeong, J.-S. Yun, Electric field induced polarization and strain of (Bi1/2Na1/2)TiO3–BaTiO3 ceramics, Ceramics International 41(3) (2015) 4789-4797.

[16] R. Cheng, Z. Xu, R. Chu, J. Hao, J. Du, G. Li, Electric field-induced ultrahigh strain and large piezoelectric effect in Bi 1/2 Na 1/2 TiO 3 -based lead-free piezoceramics, Journal of the European Ceramic Society 36(3) (2016) 489-496.

[17] H. Tao, J. Wu, Giant piezoelectric effect and high strain response in (1− x)(K 0.45 Na 0.55)(Nb 1−y Sb y)O 3 - x Bi 0.5 Na 0.5 Zr 1−z Hf z O 3 lead-free ceramics, Journal of the European Ceramic Society 36(7) (2016) 1605-1612.

[18] Y. Zhao, J. Xu, C. Zhou, C. Yuan, Q. Li, G. Chen, H. Wang, L. Yang, High energy storage properties and dielectric behavior of (Bi0.5Na0.5)0.94Ba0.06Ti1−x(Al0.5Nb0.5)xO3 lead-free ferroelectric ceramics, Ceramics International 42(2) (2016) 2221-2226.

[19] X. Liu, F. Li, P. Li, J. Zhai, B. Shen, B. Liu, Tuning the ferroelectric-relaxor transition temperature in NBT-based lead-free ceramics by Bi nonstoichiometry, Journal of the European Ceramic Society 37(15) (2017) 4585-4595.

[20] M.N. Al-Aaraji, D.A. Hall, Influence of K 0.5 Bi 0.5 TiO 3 on the structure, dielectric and ferroelectric properties of (Ba,Ca)(Zr,Ti)O 3 ceramics, Journal of the European Ceramic Society 38(5) (2018) 2344-2352.

[21] W. Zhao, R. Zuo, J. Fu, M. Shi, Large strains accompanying field-induced ergodic phase-polar ordered phase transformations in $Bi(Mg_{0.5}Ti_{0.5})O_3$–$PbTiO_3$–$(Bi_{0.5}Na_{0.5})TiO_3$ ternary system, Journal of the European Ceramic Society 34(10) (2014) 2299-2309.

[22] J. Koruza, V. Rojas, L. Molina-Luna, U. Kunz, M. Duerrschnabel, H.-J. Kleebe, M. Acosta, Formation of the core–shell microstructure in lead-free $Bi_{1/2}Na_{1/2}TiO_3$-$SrTiO_3$ piezoceramics and its influence on the electromechanical properties, Journal of the European Ceramic Society 36(4) (2016) 1009-1016.

[23] S.-Y. Cheng, J. Shieh, H.-Y. Lu, C.-Y. Shen, Y.-C. Tang, N.-J. Ho, Structure analysis of bismuth sodium titanate-based A-site relaxor ferroelectrics by electron diffraction, Journal of the European Ceramic Society 33(11) (2013) 2141-2153.

[24] H. Ogihara, C.A. Randall, S. Trolier-McKinstry, Weakly coupled relaxor behavior of $BaTiO_3$-$BiScO_3$ ceramics, Journal of The American Ceramic Society 92(1) (2009) 110-118.

[25] I. Calisir, A.A. Amirov, A.K. Kleppe, D.A. Hall, Optimisation of functional properties in lead-free $BiFeO_3$–$BaTiO_3$ ceramics through La^{3+} substitution strategy, Journal of Materials Chemistry A 6(13) (2018) 5378-5397.

[26] M. Acosta, L.A. Schmitt, L. Molina-Luna, M.C. Scherrer, M. Brilz, K.G. Webber, M. Deluca, H.-J. Kleebe, J. Rödel, W. Donner, D. Johnson, Core-shell lead-free piezoelectric ceramics: current status and advanced characterization of the $Bi_{1/2}Na_{1/2}TiO_3$-$SrTiO_3$ system, Journal of The American Ceramic Society 98(11) (2015) 3405-3422.

[27] S. Kim, G.P. Khanal, S. Ueno, C. Moriyoshi, Y. Kuroiwa, S. Wada, Revealing the role of heat treatment in enhancement of electrical properties of lead-free piezoelectric ceramics, Journal of Applied Physics 122(1) (2017) 014103.

[28] T. Miura, H. Nagata, T. Takenaka, Quenching effects on piezoelectric properties and depolarization temperatures of $(Bi_{0.5}Na_{0.5})TiO_3$-based solid solution systems, Japanese Journal of Applied Physics 56(10S) (2017) 10PD05.

[29] Q. Li, J. Wei, T. Tu, J. Cheng, J. Chen, Remarkable piezoelectricity and stable high-temperature dielectric properties of quenched $BiFeO_3$-$BaTiO_3$ ceramics, Journal of the American Ceramic Society 100(12) (2017) 5573-5583.

[30] H. Muramatsu, H. Nagata, T. Takenaka, Quenching effects for piezoelectric properties on lead-free $(Bi_{1/2}Na_{1/2})TiO_3$ceramics, Japanese Journal of Applied Physics 55(10S) (2016) 10TB07.

[31] I. Calisir, D.A. Hall, Chemical heterogeneity and approaches to its control in $BiFeO_3$–$BaTiO_3$ lead-free ferroelectrics, Journal of Materials Chemistry C 6(1) (2018) 134-146.

[32] M. Sutapun, W. Vittayakorn, RangsonMuanghlua, N. Vittayakorn, High piezoelectric response in the new coexistent phase boundary of $0.87BaTiO_3$–$(0.13-x)BaZrO_3$–$xCaTiO_3$, Materials & Design 86 (2015) 564-574.

[33] D.S. Keeble, F. Benabdallah, P.A. Thomas, Mario Maglione, J. Kreisel, Revised structural phase diagram of $(Ba_{0.7}Ca_{0.3}TiO_3)$-$(BaZr_{0.2}Ti_{0.8}O_3)$, Applied Physics Letters 102(9) (2013) 092903.

[34] Y. Tian, X. Chao, L. Jin, L. Wei, P. Liang, Z. Yang, Polymorphic structure evolution and large piezoelectric response of lead-free $(Ba,Ca)(Zr,Ti)O_3$ ceramics, Applied Physics Letters 104(11) (2014) 112901.

[35] M. Stewart, M.G. Cain, D.A. Hall, Ferroelectric Hysteresis Measurement & Analysis, Teddington: National Physical Laboratory, 1999.

[36] E.-M. Anton, W. Jo, D. Damjanovic, J. Rödel, Determination of depolarization temperature of $(Bi_{1/2}Na_{1/2})TiO_3$-based lead-free piezoceramics, Journal of Applied Physics 110(9) (2011) 094108.

[37] S.P. Thompson, J.E. Parker, J. Potter, T.P. Hill, A. Birt, T.M. Cobb, F. Yuan, C.C. Tanga, Beamline I11 at diamond: a new instrument for high resolution powder diffraction, Rev Sci Instrum 80(7) (2009) 075107.

[38] S.P. Thompson, J.E. Parker, J. Marchal, J. Potter, A. Birt, F. Yuan, R.D. Fearn, A.R. Lennie, S.R. Street, C.C. Tang, Fast X-ray powder diffraction on I11 at Diamond, J Synchrotron Radiat 18(Pt 4) (2011) 637-48.

[39] Diffrac.Suite TOPAS v. 5.0 (User Manual), BRUKER AXS GmbH, Karlsruhe (2014).

[40] H.R. Favarim, A. Michalowicz, J.C. M'Peko, V.R. Mastelaro, Phase-transition studies of $Ba_{0.90}Ca_{0.10}(Ti_{1-x}Zr_x)O_3$ ferroelectric ceramic compounds, Physica Status Solidi (A) 207(11) (2010) 2570-2577.

[41] I.K. Jeong, J.S. Ahn, The atomic structure of lead-free $Ba(Zr_{0.2}Ti_{0.8})O_3$-$(Ba_{0.7}Ca_{0.3})TiO_3$ by using neutron total scattering analysis, Applied Physics Letters 101(24) (2012) 242901.

[42] A. Zeb, S.J. Milne, S. Zhang, Stability of high-temperature dielectric properties for $(1-x)Ba_{0.8}Ca_{0.2}TiO_3$-$xBi(Mg_{0.5}Ti_{0.5})O_3$ ceramics, Journal of the American Ceramic Society 96(9) (2013) 2887-2892.

[43] A. Zeb, S.J. Milne, Low variation in relative permittivity over the temperature range 25–450°C for ceramics in the system $(1-x)[Ba_{0.8}Ca_{0.2}TiO_3]$–$x[Bi(Zn_{0.5}Ti_{0.5})O_3]$, Journal of the European Ceramic Society 34(7) (2014) 1727-1732.

[44] M.H. Lee, D.J. Kim, J.S. Park, S.W. Kim, T.K. Song, M.H. Kim, W.J. Kim, D. Do, I.K. Jeong, High-performance lead-free piezoceramics with high Curie temperatures, Advanced materials 27(43) (2015) 6976-82.

[45] D.S. Kim, C.I. Cheon, S.S. Lee, J.S. Kim, Effect of cooling rate on phase transitions and ferroelectric properties in $0.75BiFeO_3$-$0.25BaTiO_3$ ceramics, Applied Physics Letters 109(20) (2016) 202902.

[46] J.Y. Li, R.C. Rogan, E. Ustundag, K. Bhattacharya, Domain switching in polycrystalline ferroelectric ceramics, Nature materials 4(10) (2005) 776-81.

[47] L. Jin, Broadband dielectric response in hard and soft PZT: understanding softening and hardening mechanisms, PhD Thesis, SwissFederal Institute of Technology-EPFL, Switzerland, 2011.

[48] S. Liu, R.E. Cohen, Multiscale simulations of defect dipole–enhanced electromechanical coupling at dilute defect concentrations, Applied Physics Letters 111(8) (2017) 082903.

[49] L. Jin, F. Li, S. Zhang, D.J. Green, Decoding the Fingerprint of Ferroelectric Loops: Comprehension of the Material Properties and Structures, Journal of The American Ceramic Society 97(1) (2014) 1-27.

[50] R. Kiyanagi, T. Yamazaki, Y. Sakamoto, H. Kimura, Y. Noda, K. Ohyama, S. Torii, M. Yonemura, J. Zhang, T. Kamiyama, Structural and magnetic phase determination of $(1-x)BiFeO_3$–$xBaTiO_3$ solid solution, Journal of the Physical Society of Japan 81(2) (2012) 024603.

[51] M. Soda, M. Matsuura, Y. Wakabayashi, K. Hirota, Superparamagnetism induced by polar nanoregions in relaxor ferroelectric $(1-x)BiFeO_3$–$xBaTiO_3$, Journal of the Physical Society of Japan 80(4) (2011) 043705.

[52] A. Ullah, H.B. Gul, A. Ullah, M. Sheeraz, J.-S. Bae, W. Jo, C.W. Ahn, I.W. Kim, T.H. Kim, Giant room-temperature electrostrictive coefficients in lead-free relaxor ferroelectric ceramics by compositional tuning, APL Materials 6(1) (2018) 016104.